mater.scichina.com link.springer.com

Published online 14 September 2023 | https://doi.org/10.1007/s40843-023-2554-x
Sci China Mater 2023, 66(10): 3865–3874

Molecular iron phthalocyanine catalysts on morphology-engineered graphene towards the oxygen reduction reaction

Man Gao[1†], Jingjing Liu[1†], Gonglan Ye[1*], Zhongkun Zhao[2], Jianbin Liu[1], Guanchao He[1], Zhichao Gong[1], Kang Huang[1], Hongtao Sun[2*] and Huilong Fei[1*]

ABSTRACT **Molecular catalysts dispersed on nanocarbon substrates represent a unique class of single atom catalysts (SACs) for their well-defined active sites and tailorable structures, and are promising substitutes to precious metals for catalyzing the technologically important oxygen reduction reaction (ORR). Herein, we develop a highly active ORR catalyst consisting of iron phthalocyanine uniformly and densely dispersed on puff-like graphene (FePc/PG). With the unique crumpled and spheroid morphology, the graphene carrier possesses a large surface area and multiscale porosity, benefiting the high-density loading of FePc, exposure of the active sites and mass transfer efficiency during catalysis. When evaluated by a rotating disk electrode, FePc/PG presents a high half-wave potential of 0.909 V *vs.* the reversible hydrogen electrode. Furthermore, when employed as the gas diffusion electrode, FePc/PG exhibits outstanding high-rate and high-power capabilities at practically high current densities. This work provides efficient strategies to engineer the morphology of the nanocarbon substrates to design high-performance heterogeneous molecular catalysts toward applications in diverse energy conversion and storage technologies.**

Keywords: graphene, single atom catalyst, iron phthalocyanine, morphology engineering, oxygen reduction reaction

INTRODUCTION

With the purpose of mitigating the energy crisis and environmental pollution, renewable energy conversion and storage devices such as fuel cells and metal-air batteries are drawing tremendous attention [1,2]. Unfortunately, practical applications of these devices are limited by the sluggish kinetics of the associated electrochemical reactions, particularly the oxygen reduction reaction (ORR) that involves four-electron transfer processes [3]. The improvement in the efficiency of the ORR requires the use of high-performance electrocatalysts. In this regard, platinum-group metal (PGM) electrocatalysts possess exceptional activity, but their low earth abundance and high cost greatly restrain the large-scale implantation [4,5]. Therefore, it is of vital importance to develop PGM-free alternatives that combine high performance with cost-effectiveness.

Metal- and nitrogen-doped nanocarbons (M–N–Cs) with atomically dispersed M–N_x moieties have emerged as the most promising candidates for replacing PMG catalysts in catalyzing the ORR [6–10]. M–N–Cs are commonly synthesized by thermal pyrolysis at high temperature (e.g., >600°C) and they typically suffer from structural and compositional heterogeneity [11–15]. Consequently, it is challenging to control and identify the structures of the active sites, which further prevents the rational design and performance optimization of the M–N–C catalysts. Moreover, the metal atoms in M–N–Cs tend to aggregate during pyrolytic synthesis or be buried within the carbon matrix, resulting in low metal utilization efficiency during catalytic processes [16–19]. To circumvent these issues, one effective way is to use macrocycle complexes (e.g., metalated phthalocyanine and porphyrin) as molecular analogues of M–N–Cs [20–23]. Such complexes are comprised of central metal ions and macrocyclic ligands, with well-defined and uniform M–N_4 moieties that are beneficial to the identification of active sites and mechanism investigation [24–26]. Meanwhile, the high structural flexibility of the macrocycle complexes facilitates the tailoring of their physical and chemical properties by tuning the periphery substituents, which is central to improve the catalytic performance of the metal sites [26,27]. However, the aggregation and non-conducting nature of the macrocycle complexes limits their electrocatalytic performances, particularly at high current densities [22,28–30]. Therefore, it is of practical importance to support these molecular catalysts on nanocarbon materials (e.g., graphene, carbon nanotubes, and porous carbons) *via* the pyrolysis-free anchoring strategy by making use of the π–π interaction, not only to improve the electrical conductivity but also to ensure their high dispersion for enhanced exposure of active sites. In addition, the synergy between the nanocarbon substrates and molecular catalysts could lead to enhanced catalytic activity and stability [31–33].

Among various nanocarbon materials as supports for loading molecular catalysts, graphene stands out due to its unique characteristics: (i) the open two-dimensional structure and large specific surface area (SSA) are beneficial for loading and exposing high-density active sites [34]; (ii) the high electrical

[1] Advanced Catalytic Engineering Research Center of the Ministry of Education, State Key Laboratory for Chemo/Biosensing and Chemometrics, and College of Chemistry and Chemical Engineering, Hunan University, Changsha 410082, China
[2] The Harold & Inge Marcus Department of Industrial & Manufacturing Engineering, Materials Research Institute (MRI), The Pennsylvania State University, University Park 16802, Pennsylvania, USA
† These authors contributed equally to this work.
* Corresponding authors (emails: glye@hnu.edu.cn (Ye G); hzs5373@psu.edu (Sun H); hlfei@hnu.edu.cn (Fei H))

conductivity enables the continuous and rapid transport of electrons to the catalytic centers [35]; (iii) the extended π-electron system facilitates the adsorption of macrocycle complexes [36]. As the most common derivative of graphene, graphene oxide (GO) can be synthesized *via* facile solution-based processes, making it attractive as graphene precursors to be employed in applications where large-scale manufacturing of materials and devices are required [37]. Therefore, GO is considered as an excellent substrate for anchoring macrocycle complexes toward the electrocatalytic applications and its reduced form (i.e., reduced GO (rGO)) is most frequently used for its restored sp^2 domains and improved electrical conductivity [38]. Unfortunately, the transformation of GO into rGO *via* the chemical or thermal reduction methods would typically result in the irreversible restacking of graphene sheets and shrinkage in the surface area, which would adversely affect the high dispersion of macrocycle complexes and the mass transport efficiency during catalysis [20,39,40].

Herein, by making use of the combinational treatments of spray drying and thermal shock, we synthesized puff-like rGO (PG) support for loading iron phthalocyanine (FePc/PG) *via* a facile impregnation process. The unique morphologic and nanostructured features of the PG support largely alleviate the restacking-associated issues of rGO, presenting significantly enhanced Brunauer–Emmett–Teller (BET) surface area (29-fold enhancement compared with the stacked counterpart) and electrochemically active surface area (ECSA) (73-fold enhancement). Further, the PG support provides increased number of anchoring sites for dispersing the FePc molecules with facilitated exposure of active sites and mass transport during catalysis. With the combined merits, when evaluated with a rotating disk electrode (RDE), FePc/PG presents a remarkable ORR activity with a half-wave potential ($E_{1/2}$) of 0.909 V (*vs.* reversible hydrogen electrode (RHE)) and a large kinetics current (j_k = 89.2 mA cm^{-2} at 0.80 V), superior to the commercial Pt/C. Besides, when evaluated with a gas diffusion electrode (GDE), FePc/PG exhibits practically high current densities with a low mass-transport overpotential in the three-electrode configuration and a high peak power density of 228 mW cm^{-2} in a zinc-air battery (ZAB).

EXPERIMENTAL SECTION

Materials

Graphite powder (50 mesh, 99.5%) was obtained from XFNANO. Iron(II) phthalocyanine (FePc) was purchased from Aladdin Reagent. Concentrated sulfuric acid (H_2SO_4, 98.3%), fuming nitric acid (HNO_3), hydrogen peroxide (H_2O_2, 30%), hydrochloric acid (HCl, 36%–38%), potassium permanganate ($KMnO_4$, 99.5%) and ethanol (CH_3CH_2OH, ≥99.7%) were purchased from China National Medicines Co., Ltd. Potassium hydroxide (KOH, >90%) was bought from Shanghai Macklin Biochemical. Nafion 117 solution (5 wt%) was bought from Sigma-Aldrich. Carbon fiber paper (CFP, HCP120) was purchased from Shanghai Hesen. All these chemicals were used as received without any further purification.

Synthesis of rGO supports

Firstly, GO was prepared according to a modified Hummers' method [37]. An aqueous suspension of GO (1 mg mL^{-1}, 1000 mL) was magnetically stirred for 1 h, and then spray-dried with a spray dryer (ADL311, Yamato), where the inlet temperature, hot air flow rate, atomization pressure and liquid feed rate were set as 130°C, 0.38 m^3 min^{-1}, 0.10 MPa and 8.2 mL min^{-1}, respectively. After this treatment, the brownish crumpled GO (CGO) was formed and collected in a glass tank after cyclone separation. Then, CGO went through a thermal shock treatment to obtain PG with blackish color. Specifically, a homemade container loaded with CGO was quickly inserted into the heating zone of a quartz tube furnace that was pre-purged with Ar and pre-heated to 800°C by a magnetic rod and annealed for 90 min. PG was obtained after the furnace was cooled naturally to room temperature. As control samples, crumpled rGO (CG) was prepared following the same procedures except that the thermal shock treatment was substituted with a slow heating process at 5°C min^{-1}; stacked rGO (SG) was obtained by replacing the spay drying with conventional oven drying (70°C) and the thermal shock treatment with a slow heating process at 5°C min^{-1}.

Preparation of FePc/rGO hybrid materials

To prepare FePc/PG, PG (6.0 mg) was dispersed in ethanol (20 mL) and FePc (0.7 mg) was dispersed in ethanol (23 mL) by a ultrasonic homogenizer (SCIENTZ-ⅡD) for 30 and 10 min, respectively. Subsequently, FePc suspension was added to the PG suspension drop by drop. Then, the mixed dispersion was sonicated for 30 min and additionally stirred for 12 h. Lastly, the solid materials in the solution were separated by centrifuge and washed with ethanol for six times, followed by lyophilization to obtain FePc/PG. FePc/CG and FePc/SG were prepared by the similar procedure as FePc/PG.

Characterizations

Field-emission scanning electron microscopy (SEM, JSM-7610FPLUS) and transmission electron microscopy (TEM, FEI Titan G2 60-300) were used to study the morphology of the catalysts. Annular dark-field scanning TEM (ADF-STEM) was performed on a JEOL ARM300 CF with JEOL ETA aberration correctors with a beam energy of 80 keV, a 40 μm condenser lens aperture (32 mrad), an ADF detector (inner angle 47 mrad), and a beam current of approximately 46 pA. X-ray diffraction (XRD) patterns were collected on Miniflex600 with Cu Kα radiation, λ = 1.5406 Å, 40 kV and 40 mA. The pore and defective features of the catalysts were characterized by nitrogen physisorption at 77.3 K by Micromeritics ASAP 2460 and Raman spectra (InVia, 532 nm). Inductively coupled plasma mass spectrometry (ICP-MS) (Agilent 7900) was used to determine the metal content. Fourier transform infrared spectroscopy (FT-IR) measurements were measured with a Thermo Scientific NICOLET iS20.

Electrochemical measurements

All the electrochemical measurements were performed in 0.1 mol L^{-1} KOH on a CHI 760E electrochemical workstation (Chenhua, Shanghai, China) with a traditional three-electrode system with a glassy carbon electrode (5 mm in diameter), Hg/HgO electrode and graphite rod as the working electrode, reference electrode and counter electrode, respectively. To prepare the working electrode, 2 mg catalyst was added into a mixture of 940 μL alcohol and 60 μL Nafion (5 wt%). After sonicating for 60 min, 18 μL suspension was dropped on the glassy carbon electrode (0.183 mg cm^{-2}) for measurements. For

reference purpose, an electrode based on Pt/C (20 wt%) (0.142 mg cm^{-2}) catalyst ink was prepared with the similar protocol. Cyclic voltammetry (CV) was tested in the potential range of 0.2–1.2 V *vs.* RHE with a scan rate of 200 mV s^{-1}. The linear sweep voltammetry (LSV) measurements were performed with RDE and rotating ring disk electrode (RRDE, Pine Research Instrumentation) at the rotating speeds varying from 400 to 1600 r min^{-1} with a scan rate of 5 mV s^{-1} in O_2-saturated 0.1 mol L^{-1} KOH. All LSV curves were corrected with background currents that were collected in N_2-saturated 0.1 mol L^{-1} KOH. The electrochemical double-layer capacitance (C_{dl}) was derived from CV curves at the non-faradaic region (from 0.94 to 1.04 V *vs.* RHE) at various scan rates of 20, 40, 60, 80 and 100 mV s^{-1}. All potentials derived by the RDE test in 0.1 mol L^{-1} KOH were converted to RHE scale by $E_{RHE} = E_{Hg/HgO} + 0.890$ based on the calibration results (Fig. S1), and corrected with 95% *iR*-compensation.

To probe the ORR kinetics, Koutecky–Levich (K–L) plots were obtained from the following equations:

$$1/j = 1/j_L + 1/j_k = 1/B\omega^{\frac{1}{2}} + 1/j_k, \quad (1)$$

$$B = 0.62nFC_0(D_0)^{\frac{2}{3}}V^{-\frac{1}{6}}, \quad (2)$$

where j is the measured current density; j_L and j_k are the diffusion-limited current density and kinetics current density, respectively; ω is the angular velocity; n is the transferred electron number; F is the Faraday constant (96,485 C mol^{-1}); C_0 is the bulk concentration of O_2 (1.15×10^{-6} mol cm^{-3}); D_0 is the diffusion coefficient of O_2 in 0.1 mol L^{-1} KOH (1.9×10^{-6} cm^2 s^{-1}); V is the kinetics viscosity of the electrolyte (0.01 cm^2 s^{-1}). The electron transfer number (n) and hydrogen peroxide yield (H_2O_2%) were evaluated by the following two equations with RRDE tests:

$$H_2O_2\% = 200 \times (i_r/N)/(i_d + i_r/N), \quad (3)$$

$$n = 4 \times i_d/(i_d + i_r/N), \quad (4)$$

where i_r and i_d are the ring and disk current densities, respectively. N is the ring current collection efficiency, which was calibrated to be 37%.

The ECSA for different samples with mass loading of 0.183 mg cm^{-2} was estimated from the electrochemical double-layer capacitance (C_{dl}), which was determined from the CVs at the scan rates of 20, 40, 60, 80 and 100 mV s^{-1} in a non-faradaic potential range of 0.94 to 1.04 V *vs.* RHE. The ECSA was calculated according to Equation (5):

$$ECSA = R_f/\text{mass loading}, \quad (5)$$

where R_f is the roughness factor that was calculated from C_{dl} according to Equation (6) [41]:

$$R_f = C_{dl}/C_s, \quad (6)$$

where C_s is the specific capacitance (generally in the range of 20 to 60 μF cm^{-2}) of a flat standard electrode and the averaged value of 40 μF cm^{-2} was used here for the calculation [7].

Mass activity (MA) and turnover frequency (TOF) were calculated by the following equations assuming each metal atom constituting one active site for the ORR:

$$MA = j_k/L_{cat}\omega_{Fe}, \quad (7)$$

$$TOF = j_kM_{Fe}/L_{cat}\omega_{Fe}F, \quad (8)$$

where j_k is the kinetics current density calculated from the K–L equation, M_{Fe} is the molar mass of Fe, $L_{cat.}$ is the mass loading of the catalyst on the electrode, ω_{Fe} is the Fe content in the catalysts, and F is the Faraday constant.

Half-cell test with GDE

An electrochemical workstation (Admiral) was used to evaluate the electrocatalytic activity in a three-electrode electrochemical test system, which consisted of a carbon paper electrode covered with a catalyst film (1.00 cm^2, the working electrode), a graphite rod (the counter electrode), and a Hg/HgO electrode (the reference electrode). To prepare the GDE, catalyst ink consisting of 4 mg electrocatalysts, 940 μL alcohol and 60 μL Nafion (5 wt%) were drop-casted on a CFP (HCP120) and dried at room temperature for 1 h. The catalyst loadings were controlled at 0.8 mg cm^{-2}. The electrochemical measurements were conducted in 1.0 mol L^{-1} KOH solution. All the potentials were converted to RHE scale by $E_{RHE} = E_{Hg/HgO} + 0.926$ based on the calibration results in 1.0 mol L^{-1} KOH (Fig. S2), and all potentials were corrected with 50% *iR*-compensation.

Assembling and testing of ZAB

The ZAB was composed of a Zn plate (thickness: 0.5 mm; purity: 99.99%) as the anode, 6 mol L^{-1} KOH aqueous solution as the electrolyte and a catalyst layer as the cathode. The cathode catalyst layer was prepared by uniformly dropping catalyst ink onto CFP (HCP120, diameter: 15 mm) and then dried at room temperature for 1 h. The cathode catalyst loadings for all samples were kept at 0.8 mg cm^{-2} but the Pt/C catalyst was at 0.4 mg cm^{-2}. An electrochemical workstation (Admiral) was used to measure the discharge polarization curves at a sweep rate of 10 mV s^{-1} without *iR* correction. The discharge platforms were obtained by a LANHE instrument electrochemical workstation (CT2001A) at room temperature. All tests were performed under 25 standard cubic centimeter per minute (sccm) O_2 (purity: >99.9%). The power density (P) was calculated as follows:

$$P = IV, \quad (9)$$

where I is the discharge current density and V is the corresponding voltage.

RESULTS AND DISCUSSION

Synthesis and characterization of the graphene supports

PG was synthesized *via* the combinational treatments of spray drying and thermal shock with GO as the precursor (Fig. 1). Briefly, an aqueous GO solution firstly went through an aerosol spray drying process, during which the GO nanosheets were transformed into crumpled particles as a result of the capillary compression force [42,43]. Then, the crumpled GO solid was reduced with a thermal shock (T-shock) treatment to result in PG with puffy spheroid-like morphology. The morphology transformation during this T-shock step could be ascribed to the instant release of the gases (e.g., CO_2, CO, and H_2O) from the decomposition of the oxygen-containing functional groups in GO [44], leading to the accumulation of high pressure within the free space of the structure that ultimately resulted in "nanoscale explosion" to cause the expansion of the graphene layers, as evidenced by the large sample volume increase after the T-shock (Fig. S3). These two-step treatments incorporated within the synthetic design were found to be indispensable in achieving the unique morphologic and structural features of PG. To illustrate the necessity for each step, two control samples were prepared, including CG prepared with spray drying and slow heating

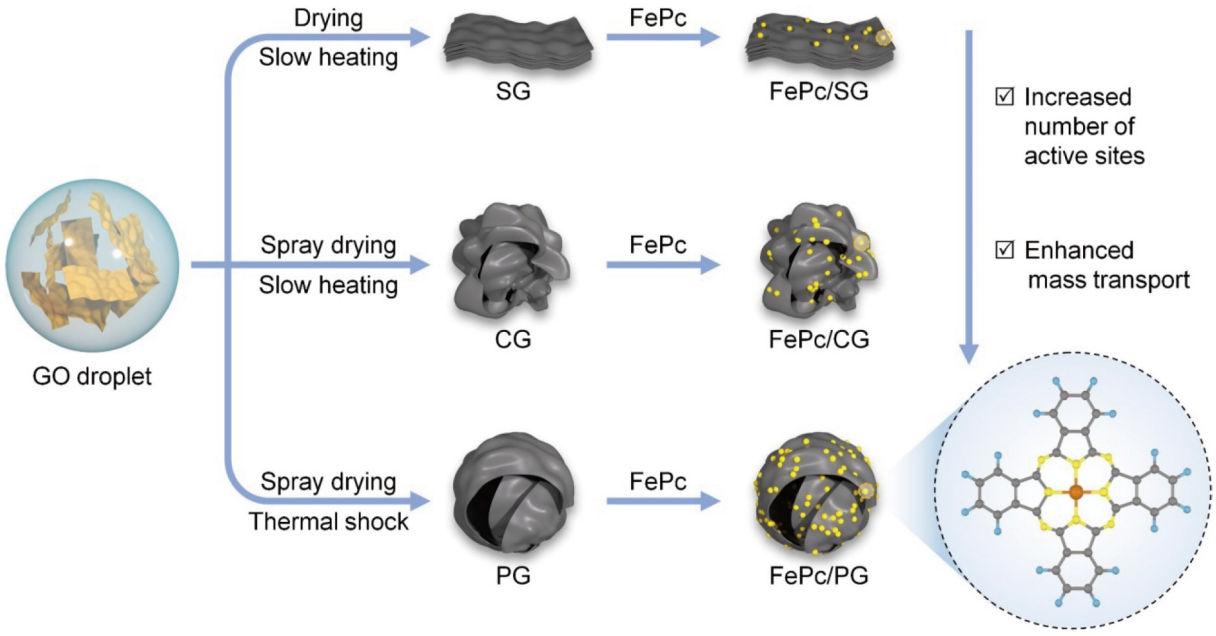

Figure 1 A schematic description of the synthetic approaches to SG, CG and PG, and the corresponding hybrid catalysts of FePc/SG, FePc/CG and FePc/PG.

treatments, and SG with oven drying and slow heating treatments. The detailed synthetic procedures for PG, CG and SG were described in the EXPERIMENTAL SECTION.

The morphologic features of PG, CG and SG were firstly characterized by SEM (Fig. 2a–f). It is evident that PG possesses a puffy spheroid-like shape (Fig. 2a, d), and the particle size distribution analysis suggests that PG has a particle size of 2.34 ± 0.78 μm (Fig. S4). For CG, it is in crumpled ball-like morphology with abundant sharp ridges and folds (Fig. 2b, e). The particle size of CG is 1.21 ± 0.33 μm, significantly smaller than that of PG, ascribing to the structural expansion induced by the T-shock treatment for preparing PG. For SG, it exhibits a flake-like and smooth appearance and the graphene sheets are tightly stacked to form thick platelets (Fig. 2c, f). TEM characterizations on the individual particles confirm the above observations (Fig. 2g–i). Additionally, among the three samples, the graphene layers in PG are most loosely packed and they appear to be thinnest with high electron transparency.

XRD patterns reveal that all three samples display two broad peaks at ~26° and ~44°, corresponding to the (002) and (101) planes of graphitic carbon (Fig. 3a). The presence of the broader (002) peak for PG as compared with the other samples implies that the graphene nanosheets are arranged in a more disordered and random manner with low crystallinity, which is caused by the T-shock treatment [44]. In comparison, the (002) peak for SG is relatively sharp due to the severe re-stacking encountered during the drying and thermal reduction processes. BET surface area analysis shows that PG has a surface area of 333 $m^2 g^{-1}$, which is much higher than CG (131 $m^2 g^{-1}$) and SG (11 $m^2 g^{-1}$) (Fig. 3b). In addition, PG and CG both display a pseudo-type-I adsorption/desorption isotherm with a hysteresis loop at high pressure and a type IV isotherm with a hysteresis loop at moderate pressure, indicating the presence of well-developed mesopores and macropores [44,45], while, in strong contrast, SG is lacking of these features in the isotherm profiles, implying its poor porosity. The pore-size distribution curves in Fig. 3c show that PG possesses enriched nanopores with size dominated in the range of ~10–100 and ~1 nm, and it has a significantly increased total pore volume of 0.687 $cm^3 g^{-1}$, much high than CG (0.153 $cm^3 g^{-1}$) and SG (0.012 $cm^3 g^{-1}$) (Table S1). Moreover, the ECSA of PG, CG and SG were estimated from the double-layer capacitance (C_{dl}) measured in the non-faradaic potential region (Fig. 3d and Fig. S5). The results show that the ECSA of PG (80.1 $m^2 g^{-1}$) is significantly higher than CG (31.7 $m^2 g^{-1}$) and SG (1.04 $m^2 g^{-1}$), highlighting the beneficial role of the puffy-spheroid morphology of PG in exposing the electrode/electrolyte interfaces.

Preparation and characterization of the hybrid catalysts

The FePc molecules were dispersed onto different graphene supports to obtain hybrid catalysts including FePc/SG, FePc/CG and FePc/PG *via* a facile pyrolysis-free impregnation method by making use of the π–π stacking interaction between FePc and the graphene substrates (Fig. 1). The morphologic features of these composites were similar to those of the corresponding bare supports (Fig. S6), highlighting that the structures are mechanically robust against the possible collapse induced by the intensive ultrasonic treatment used for impregnation. The Fe contents of the three catalysts were determined by ICP-MS. As summarized in Fig. 4a, the Fe contents for FePc/PG, FePc/CG and FePc/SG are 1.13, 0.22 and 0.11 wt%, respectively. The significantly higher Fe loading content in FePc/PG can be attributed to the large surface area, open structure and high porosity of the PG support, which provides abundant anchoring sites for dispersing high density of FePc molecules. In comparison, the SG with low surface area and compact structure disfavors the dispersion of the FePc molecules, resulting in ~10 times lower Fe content. For the XRD patterns of FePc/SG, FePc/CG and FePc/PG (Fig. 4b), the peaks at ~7° and ~15.5° corresponding to the (100) and (200) planes of the crystalline FePc

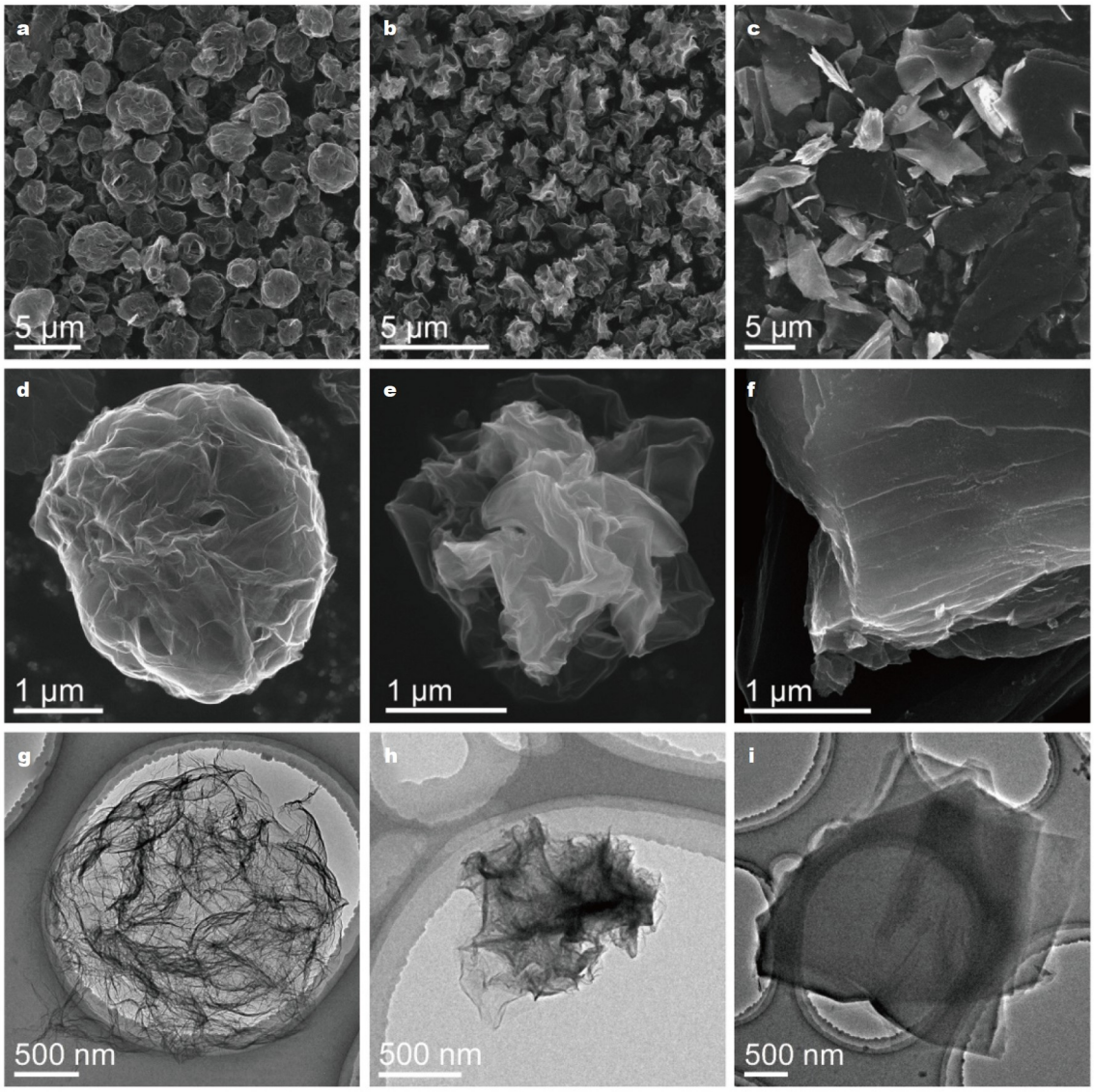

Figure 2 Low-magnification (a–c) and high-magnification (d–f) SEM images of PG, CG and SG, respectively. (g–i) TEM images of PG, CG and SG, respectively.

were not observed [46], indicating the uniform distribution of the individual FePc molecules. Raman spectra suggest that only the D and G bands of the graphene substrates are present in FePc/PG, FePc/CG and FePc/SG while the vibration modes characteristic of the pure FePc are absent (Fig. 4c), which could be ascribed to the strong electronic coupling between the FePc molecules and the substrates [29,47]. From the FT-IR (Fig. 4d and Fig. S7), the vibration mode of the Fe–N bond at 1162 cm^{-1} shows up in all three catalysts, confirming the successful loading of the FePc molecules on the graphene carriers, but the signal in FePc/CG is weak due to its low loading content of FePc. Additional absorption peaks at 721, 1118 and 1467 cm^{-1}, assigned to the C–H bending out of the plane deformations in FePc, are present in all catalysts and the pure FePc [46,48]. However, it should be noted that compared with the pure FePc, the peaks at ~721 cm^{-1} for the three catalysts blue shift to higher wavenumbers, resulting from the π–π interaction between FePc and the substrate [49]. Furthermore, ADF-STEM image shows that the Fe metals in FePc/PG are atomically dispersed on the graphene substrate (Fig. 4e). Energy-dispersive X-ray spectroscopy (EDS) mapping images reveal that the C, N, and Fe elements distribute uniformly on the substrate in FePc/PG (Fig. 4f).

ORR performance evaluated by the RDE technique

The ORR activity of the catalysts was firstly evaluated by the RDE technique with a typical three-electrode configuration in 0.1 mol L^{-1} KOH. It is noted that the ORR activity of FePc/PG has been optimized by adjusting the T-shock temperatures (Fig. S8). Fig. 5a presents the CV curves of PG, FePc/SG, FePc/CG and FePc/PG, along with commercial Pt/C as reference, in O_2- and N_2-saturated electrolytes. In N_2-saturated electrolyte, a pair of redox peaks at 0.65–0.95 V was observed in FePc/PG that can be indexed to the reduction/oxidation peaks of Fe^{3+}/Fe^{2+} [50], while these peaks are quite weak in FePc/CG and FePc/SG as a result of the low loading contents of FePc. In O_2-saturated electrolyte, an obvious O_2 reduction peak was observed in all

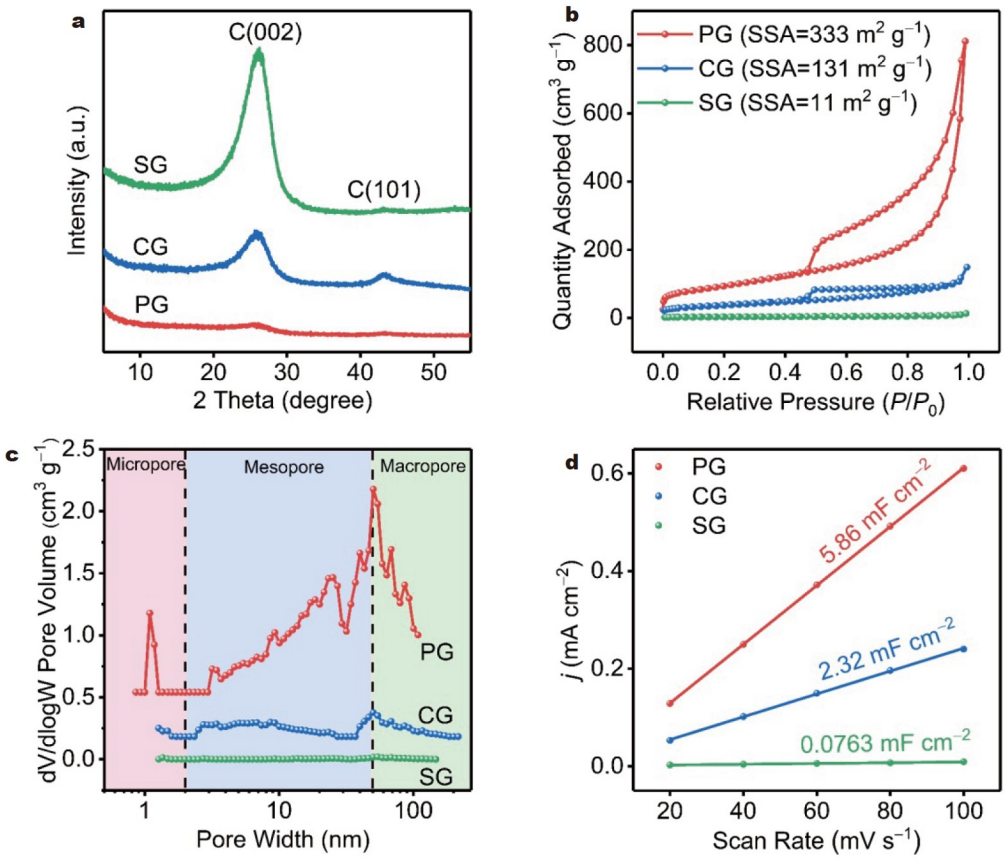

Figure 3 (a) XRD patterns, (b) N_2 adsorption/desorption isotherms, (c) pore-size distribution curves, and (d) electrochemical double layer capacitance (C_{dl}) for PG, CG and SG.

measured catalysts. Notably, FePc/PG displays the highest cathodic peak current density and most positive reduction peak position, followed by FePc/CG and FePc/SG. For the bare PG, its reduction peak position is least positive, indicative of its low ORR activity, highlighting the critical role of the dispersed FePc molecules in enhancing the activity. As shown by the LSV curves in Fig. 5b, FePc/PG delivers the highest ORR activity with a high half-wave potential ($E_{1/2}$) of 0.909 V, which is much positive than Pt/C (0.862 V), FePc/CG (0.790 V), FePc/SG (0.734 V) and PG (0.725 V), and better than most of the nanocarbon-supported FePc catalysts reported so far (Table S2). The superiority of the PG support was also demonstrated by the better activity of FePc/PG compared with the hybrid catalyst consisting of FePc supported on commercial carbon black (Fig. S9). In addition, FePc/PG exhibits calculated kinetics current densities (j_k) of 85.20 and 53.90 mA cm^{-2} at 0.80 and 0.85 V, respectively, superior to Pt/C (45.10 and 7.85 mA cm^{-2}), FePc/CG (3.21 and 0.55 mA cm^{-2}), FePc/SG (1.19 and 0.27 mA cm^{-2}) and PG (0.42 and 0.04 mA cm^{-2}) (Fig. 5c). At the same time, FePc/PG presents an extraordinary Tafel slope of 28.2 mV dec^{-1}, which is notably lower than Pt/C (57.1 mV dec^{-1}), FePc/CG (97.2 mV dec^{-1}), FePc/SG (178.6 mV dec^{-1}) and PG (52.1 mV dec^{-1}) (Fig. 5d), suggesting the faster ORR kinetics of FePc/PG. In addition, FePc/PG delivers higher values of MA and TOFs than FePc/SG and FePc/CG (Table S3), suggesting the higher intrinsic activity of FePc/PG. The selectivity toward the four-electron ORR for the catalysts was investigated by RRDE measurements. For FePc/PG, the electron transfer number (n) is close to 4.0 and the yield of the generated byproduct H_2O_2 is near zero in the potential range of 0.20–0.75 V (Fig. 5e), indicating that the ORR on FePc/PG follows through the four-electron reduction pathway and the main product is H_2O, similar to the case of Pt/C. K–L linear plots were also used to calculate the n values (Fig. S10), corroborating the experimental results from the RRDE measurements. In comparison, FePc/CG and FePc/SG show inferior selectivity toward the four-electron pathway (Fig. 5e). The catalytic stability of FePc/PG was evaluated by both CV cycling and chronoamperometry test. The results show that the $E_{1/2}$ of FePc/PG degrades by only 10 mV after 5000 CV cycles compared with 29 mV in Pt/C (Fig. 5f), while FePc/CG and FePc/SG decays more (Fig. S11). Meanwhile, the current of FePc/PG keeps a high retention of 91.4% after an 8-h chronoamperometry test (Fig. S12), revealing the excellent stability of FePc/PG.

ORR performance evaluated by the GDE

RDE measurement usually requires a thin-film catalyst layer on the electrode and is limited by the low solubility of the gaseous reactant in the electrolyte [51]. Therefore, it is difficult to investigate the efficient mass transport and full utilization of active sites at the three-phase interface when the RDE activity is translated into practical applications (e.g., fuel cells and ZAB) [52]. To further evaluate the electrocatalytic performance of the catalysts, half cells with the GDE were employed for overcoming the mass transport limitations and fast catalyst evaluation under practical operation conditions. From the polarization curves in

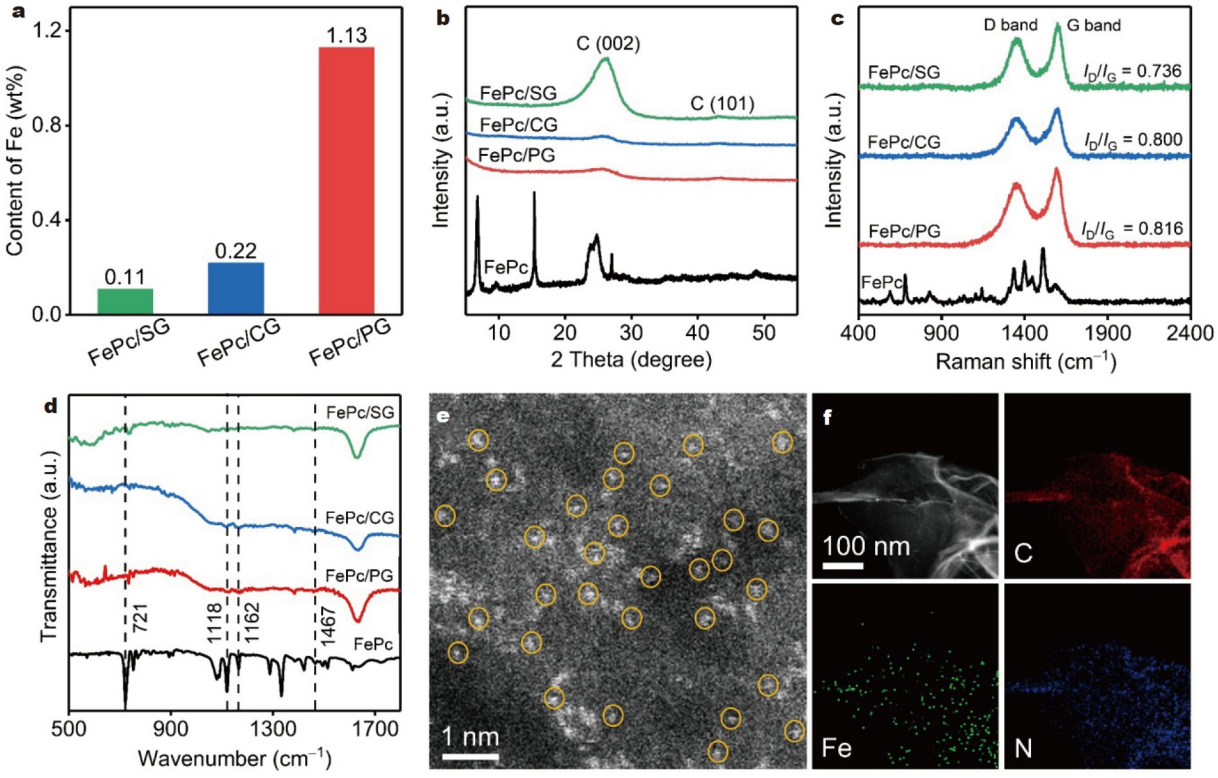

Figure 4 (a) Fe contents in FePc/SG, FePc/CG and FePc/PG determined by ICP-MS. (b) XRD patterns, (c) Raman spectra, (d) FT-IR spectra of FePc/SG, FePc/CG, FePc/PG and FePc. (e) ADF-STEM image of FePc/PG. The Fe atoms are marked by yellow circles. (f) TEM image and the corresponding EDS elemental mappings of FePc/PG.

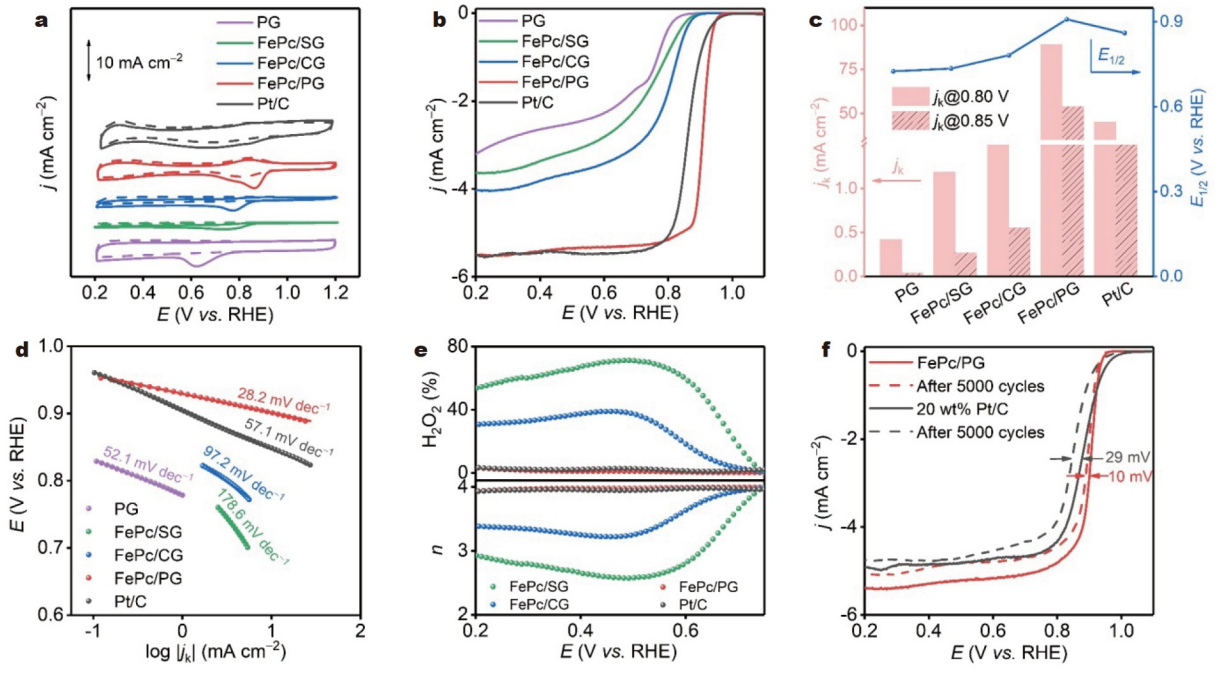

Figure 5 (a) CV in N_2 (dash) and O_2-saturated (solid) 0.1 mol L^{-1} KOH (scan rate: 200 mV s^{-1}), (b) LSV curves, (c) comparison of $E_{1/2}$ and j_k at 0.80 and 0.85 V *vs.* RHE, and (d) Tafel plots of PG, FePc/SG, FePc/CG, FePc/PG and Pt/C. (e) H_2O_2 yields and electron transfer numbers (n) of FePc/SG, FePc/CG, FePc/PG and Pt/C. (f) Stability measurements with CV methods for FePc/PG and Pt/C.

Fig. 6a, FePc/PG with an optimized loading of 0.8 mg cm^{-2} exhibits considerably high ORR activity at high current densities up to 1000 mA cm^{-2} with much smaller overpotential than FePc/CG, FePc/SG and Pt/C, contributing to its enhanced mass transport efficiency. To quantitatively compare the mass transport efficiency of FePc/PG and FePc/SG, the mass-transport

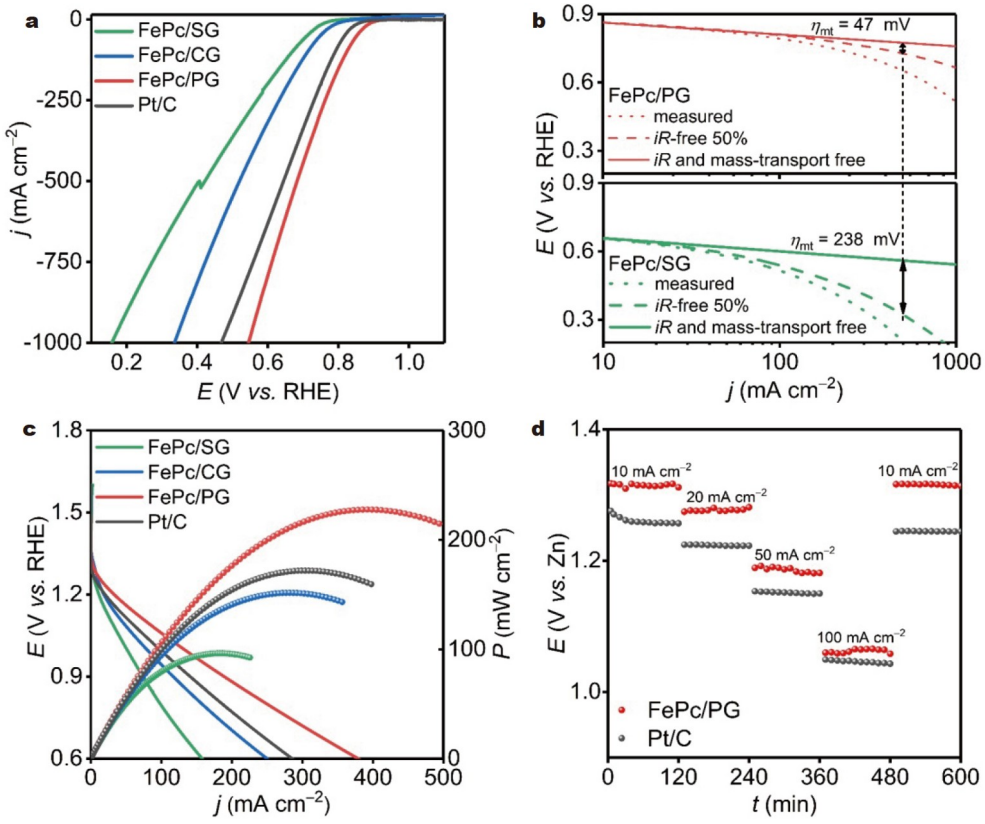

Figure 6 (a) ORR LSV polarization curves in 1.0 mol L^{-1} KOH at 10 mV s^{-1} for FePc/SG, FePc/CG, FePc/PG and Pt/C with GDEs. (b) Determination of the mass-transport overpotentials (η_{mt}) of FePc/PG and FePc/SG. (c) Discharge polarization curves and the corresponding power densities of FePc/SG, FePc/CG, FePc/PG and Pt/C in ZABs. (d) Discharge platforms of FePc/PG and Pt/C at various current densities in ZABs.

overpotentials (η_{mt}) at high current densities were extracted from the polarization curves (Fig. 6b), showing that FePc/PG possesses a η_{mt} of 47 mV at 500 mA cm^{-2}, which is much smaller than that (238 mV) of FePc/SG. Taking a step further, ZAB was assembled with the catalyst-coated GDE as the air cathode. FePc/PG exhibits a superior open circuit potential (1.47 V *vs.* Zn) to FePc/CG (1.36 V), FePc/SG (1.30 V) and Pt/C (1.41 V) (Fig. S13). From the LSV polarization plots in Fig. 6c, FePc/PG delivers a current density of 395 mA cm^{-2} at 1.51 V and a maximum power density of 227 mW cm^{-2}, outperforming FePc/CG (284 mA cm^{-2}, 152 mW cm^{-2}), FePc/SG (182 mA cm^{-2}, 96 mW cm^{-2}) and Pt/C (301 mA cm^{-2}, 172 mW cm^{-2}). The rate capability at different current densities (10, 20, 50, 100 mA cm^{-2}) is displayed in Fig. 6d. FePc/PG presents lower overpotentials than Pt/C at all current densities. It is notable that the discharge voltage plateau is completely restored when the current density returns to 10 mA cm^{-2}, showing the outstanding rate capability for the FePc/PG cathode. In short, the multiscale porous structure of FePc/PG is beneficial to the mass transport and high rate/power capability in the three-electrode half cells and two-electrode ZAB.

CONCLUSIONS

In summary, we have developed an outstanding ORR electrocatalyst consisting of FePc molecules uniformly dispersed on puff-like graphene carriers, which were synthesized through the combined treatments of spray drying and thermal shock. The unique morphologic features of the graphene substrate significantly enlarged the area of adsorption and enhanced the exposure of active sites compared with the stacked and crumpled counterpart. As a result, the optimal catalyst exhibited an outstanding ORR activity with an $E_{1/2}$ of 0.909 V *vs.* RHE, a low Tafel slope of 28.2 mV dec^{-1}, and a high kinetics current density of 59.3 mA cm^{-2} at 0.85 V, outperforming commercial Pt/C and most of the previous FePc-based carbon catalysts. Moreover, GDEs coated with the optimal catalyst exhibited high current densities up to 1000 mA cm^{-2} at relatively low overpotentials in a half-cell configuration and a high peak power density of 227 mW cm^{-2} in a ZAB. This work provides an efficient strategy to tune the morphology of carbon substrates to optimize the performance of heterogeneous molecular catalysts, enabling their applications in various energy conversion processes such as ORR, CO_2 reduction and N_2 reduction.

Received 14 June 2023; accepted 17 July 2023; published online 14 September 2023

1 Zaman S, Huang L, Douka AI, *et al.* Oxygen reduction electrocatalysts toward practical fuel cells: Progress and perspectives. Angew Chem, 2021, 133: 17976–17996
2 Peng L, Shang L, Zhang T, *et al.* Recent advances in the development of single-atom catalysts for oxygen electrocatalysis and zinc-air batteries. Adv Energy Mater, 2020, 10: 2003018
3 Nie Y, Li L, Wei Z. Recent advancements in Pt and Pt-free catalysts for oxygen reduction reaction. Chem Soc Rev, 2015, 44: 2168–2201
4 Debe MK. Electrocatalyst approaches and challenges for automotive fuel cells. Nature, 2012, 486: 43–51
5 Liu J, Jiao M, Mei B, *et al.* Carbon-supported divacancy-anchored

platinum single-atom electrocatalysts with superhigh Pt utilization for the oxygen reduction reaction. Angew Chem Int Ed, 2019, 58: 1163–1167
6 Qiao B, Wang A, Yang X, *et al.* Single-atom catalysis of CO oxidation using Pt_1/FeO_x. Nat Chem, 2011, 3: 634–641
7 Fei H, Dong J, Arellano-Jiménez MJ, *et al.* Atomic cobalt on nitrogen-doped graphene for hydrogen generation. Nat Commun, 2015, 6: 8668
8 Fei H, Dong J, Feng Y, *et al.* General synthesis and definitive structural identification of MN_4C_4 single-atom catalysts with tunable electrocatalytic activities. Nat Catal, 2018, 1: 63–72
9 Xie X, He C, Li B, *et al.* Performance enhancement and degradation mechanism identification of a single-atom Co–N–C catalyst for proton exchange membrane fuel cells. Nat Catal, 2020, 3: 1044–1054
10 Jiao L, Li J, Richard LLR, *et al.* Chemical vapour deposition of Fe–N–C oxygen reduction catalysts with full utilization of dense $Fe–N_4$ sites. Nat Mater, 2021, 20: 1385–1391
11 Hu L, Dai C, Chen L, *et al.* Metal-triazolate-framework-derived FeN_4Cl_1 single-atom catalysts with hierarchical porosity for the oxygen reduction reaction. Angew Chem Int Ed, 2021, 60: 27324–27329
12 Sa YJ, Seo DJ, Woo J, *et al.* A general approach to preferential formation of active $Fe–N_x$ sites in Fe–N/C electrocatalysts for efficient oxygen reduction reaction. J Am Chem Soc, 2016, 138: 15046–15056
13 Liu J, Gong Z, Allen C, *et al.* Edge-hosted $Fe-N_3$ sites on a multiscale porous carbon framework combining high intrinsic activity with efficient mass transport for oxygen reduction. Chem Catal, 2021, 1: 1291–1307
14 Zhang N, Zhou T, Chen M, *et al.* High-purity pyrrole-type FeN_4 sites as a superior oxygen reduction electrocatalyst. Energy Environ Sci, 2020, 13: 111–118
15 Yin P, Yao T, Wu Y, *et al.* Single cobalt atoms with precise N-coordination as superior oxygen reduction reaction catalysts. Angew Chem Int Ed, 2016, 55: 10800–10805
16 Qin R, Liu P, Fu G, *et al.* Strategies for stabilizing atomically dispersed metal catalysts. Small Methods, 2018, 2: 1700286
17 Wang XX, Swihart MT, Wu G. Achievements, challenges and perspectives on cathode catalysts in proton exchange membrane fuel cells for transportation. Nat Catal, 2019, 2: 578–589
18 Zhang H, Hwang S, Wang M, *et al.* Single atomic iron catalysts for oxygen reduction in acidic media: particle size control and thermal activation. J Am Chem Soc, 2017, 139: 14143–14149
19 Sun T, Xu L, Wang D, *et al.* Metal organic frameworks derived single atom catalysts for electrocatalytic energy conversion. Nano Res, 2019, 12: 2067–2080
20 Peng P, Shi L, Huo F, *et al.* A pyrolysis-free path toward superiorly catalytic nitrogen-coordinated single atom. Sci Adv, 2019, 5: eaaw2322
21 Chen K, Liu K, An P, *et al.* Iron phthalocyanine with coordination induced electronic localization to boost oxygen reduction reaction. Nat Commun, 2020, 11: 4173
22 Zhang X, Wang Y, Gu M, *et al.* Molecular engineering of dispersed nickel phthalocyanines on carbon nanotubes for selective CO_2 reduction. Nat Energy, 2020, 5: 684–692
23 Cao P, Quan X, Nie X, *et al.* Metal single-site catalyst design for electrocatalytic production of hydrogen peroxide at industrial-relevant currents. Nat Commun, 2023, 14: 172
24 Wan W, Triana CA, Lan J, *et al.* Bifunctional single atom electrocatalysts: Coordination-performance correlations and reaction pathways. ACS Nano, 2020, 14: 13279–13293
25 Wan L, Zhao K, Wang YC, *et al.* Molecular degradation of iron phthalocyanine during the oxygen reduction reaction in acidic media. ACS Catal, 2022, 12: 11097–11107
26 Wu Y, Liang Y, Wang H. Heterogeneous molecular catalysts of metal phthalocyanines for electrochemical CO_2 reduction reactions. Acc Chem Res, 2021, 54: 3149–3159
27 Chen K, Cao M, Lin Y, *et al.* Ligand engineering in nickel phthalocyanine to boost the electrocatalytic reduction of CO_2. Adv Funct Mater, 2021, 32: 2111322
28 Cheng W, Yuan P, Lv Z, *et al.* Boosting defective carbon by anchoring well-defined atomically dispersed metal-N_4 sites for ORR, OER, and Zn-air batteries. Appl Catal B-Environ, 2020, 260: 118198
29 Mei Z, Cai S, Zhao G, *et al.* Boosting the ORR active and Zn-air battery performance through ameliorating the coordination environment of iron phthalocyanine. Chem Eng J, 2022, 430: 132691
30 Yu X, Lai S, Xin S, *et al.* Coupling of iron phthalocyanine at carbon defect site *via* π–π stacking for enhanced oxygen reduction reaction. Appl Catal B-Environ, 2021, 280: 119437
31 Zhang L, Zhu J, Li X, *et al.* Nurturing the marriages of single atoms with atomic clusters and nanoparticles for better heterogeneous electrocatalysis. Interdisciplinary Mater, 2022, 1: 51–87
32 Wang T, Wang P, Zang W, *et al.* Nanoframes of Co_3O_4-Mo_2N heterointerfaces enable high-performance bifunctionality toward both electrocatalytic HER and OER. Adv Funct Mater, 2021, 32: 2107382
33 Paul R, Zhai Q, Roy AK, *et al.* Charge transfer of carbon nanomaterials for efficient metal-free electrocatalysis. Interdisciplinary Mater, 2022, 1: 28–50
34 Bonaccorso F, Colombo L, Yu G, *et al.* Graphene, related two-dimensional crystals, and hybrid systems for energy conversion and storage. Science, 2015, 347: 1246501
35 Geim AK, Novoselov KS. The rise of graphene. Nat Mater, 2007, 6: 183–191
36 Hong Y, Li L, Huang B, *et al.* Molecular control of carbon-based oxygen reduction electrocatalysts through metal macrocyclic complexes functionalization. Adv Energy Mater, 2021, 11: 2100866
37 Marcano DC, Kosynkin DV, Berlin JM, *et al.* Improved synthesis of graphene oxide. ACS Nano, 2010, 4: 4806–4814
38 Fei H, Dong J, Chen D, *et al.* Single atom electrocatalysts supported on graphene or graphene-like carbons. Chem Soc Rev, 2019, 48: 5207–5241
39 Si Y, Samulski ET. Exfoliated graphene separated by platinum nanoparticles. Chem Mater, 2008, 20: 6792–6797
40 Li Y, Li Y, Zhu E, *et al.* Stabilization of high-performance oxygen reduction reaction Pt electrocatalyst supported on reduced graphene oxide/carbon black composite. J Am Chem Soc, 2012, 134: 12326–12329
41 Wu K, Shi L, Wang Z, *et al.* A general strategy to generate oxygen vacancies in bimetallic layered double hydroxides for water oxidation. Chem Commun, 2023, 59: 3138–3141
42 Luo J, Jang HD, Sun T, *et al.* Compression and aggregation-resistant particles of crumpled soft sheets. ACS Nano, 2011, 5: 8943–8949
43 Cranford SW, Buehler MJ. Packing efficiency and accessible surface area of crumpled graphene. Phys Rev B, 2011, 84: 205451
44 Huang K, Wei Z, Liu J, *et al.* Engineering the morphology and microenvironment of a graphene-supported Co–N–C single-atom electrocatalyst for enhanced hydrogen evolution. Small, 2022, 18: e2201139
45 Taniguchi T, Nurdiwijayanto L, Sakai N, *et al.* Revisiting the two-dimensional structure and reduction process of graphene oxide with in-plane X-ray diffraction. Carbon, 2023, 202: 26–35
46 Liu T, Zhang F, Ruan L, *et al.* Facile synthesis and characterization of crystalline iron phthalocyanine. Mater Lett, 2019, 237: 319–322
47 Choi C, Wang X, Kwon S, *et al.* Efficient electrocatalytic valorization of chlorinated organic water pollutant to ethylene. Nat Nanotechnol, 2022, 18: 160–167
48 Zhang C, Hao R, Yin H, *et al.* Iron phthalocyanine and nitrogen-doped graphene composite as a novel non-precious catalyst for the oxygen reduction reaction. Nanoscale, 2012, 4: 7326–7329
49 Guo J, Yan X, Liu Q, *et al.* The synthesis and synergistic catalysis of iron phthalocyanine and its graphene-based axial complex for enhanced oxygen reduction. Nano Energy, 2018, 46: 347–355
50 Wei J, Xia D, Wei Y, *et al.* Probing the oxygen reduction reaction intermediates and dynamic active site structures of molecular and pyrolyzed Fe–N–C electrocatalysts by *in situ* Raman spectroscopy. ACS Catal, 2022, 12: 7811–7820
51 Inaba M, Jensen AW, Sievers GW, *et al.* Benchmarking high surface area electrocatalysts in a gas diffusion electrode: Measurement of oxygen reduction activities under realistic conditions. Energy Environ Sci, 2018, 11: 988–994
52 Huang L, Wei M, Qi R, *et al.* An integrated platinum-nanocarbon electrocatalyst for efficient oxygen reduction. Nat Commun, 2022, 13: 6703

Acknowledgements Fei H acknowledges the financial support from the National Natural Science Foundation of China (92163116) and the Major Program of the Natural Science Foundation of Hunan Province (2021JC0006). Ye G acknowledges the support from the National Natural Science Foundation of China (22209043).

Author contributions Fei H, Sun H and Ye G conceived the concept and supervised the research. Gao M and Liu J performed the experiments, analyzed the data, and wrote the original draft. He G, Gong Z and Huang K carried out SEM, XRD, ICP-MS tests. Zhao Z and Liu J conducted partial data analysis. All authors discussed the results and commented on the manuscript.

Conflict of interest The authors declare that they have no conflict of interest.

Supplementary information Supporting data are available in the online version of the paper.

Man Gao received her BE degree from the North University of China in 2020. She is currently studying for a Master's degree at the College of Chemistry and Chemical Engineering, Hunan University, China. Her main research directions are graphene-based oxygen reduction electrocatalysts and their applications.

Jingjing Liu is currently a PhD student at the College of Chemistry and Chemical Engineering, Hunan University, China. She received her MS degree from the College of Chemistry and Chemical Engineering, Central South University in 2019. Her research focuses on the design of functional nanocarbon materials for ORR in metal-air batteries and hydrogen peroxide production.

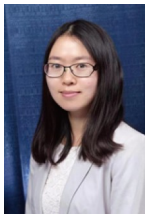

Gonglan Ye is currently an associate professor at the College of Chemistry and Chemical Engineering, Hunan University, China. She received her BS degree (2010) in materials chemistry from China University of Geoscience (Wuhan) and PhD degree (2016) in materials science and nanoengineering from Rice University. Before she joined Hunan University, she had worked as a senior packaging engineer at Intel in Chandler, Arizona (2017–2019). Her scientific interest focuses on the controllable synthesis of two-dimensional (2D) materials for energy storage and conversion.

Hongtao Sun is an assistant professor at Harold and Inge Marcus Department of Industrial and Manufacturing Engineering, Pennsylvania State University, University Park, USA. He obtained his PhD degree in mechanical engineering from Rensselaer Polytechnic Institute (RPI) in 2014. He was previously a postdoc researcher at the University of California, Los Angeles. His current research interests focus on the co-design of materials, structures, and manufacturing processes with a particular emphasis on their applications in the field of energy.

Huilong Fei is currently a professor at the College of Chemistry and Chemical Engineering, Hunan University, China. He received his BS degree in materials chemistry from China University of Geosciences (Wuhan) in 2011, and his PhD degree in chemistry from Rice University in 2015. He was previously a postdoc researcher at the University of California, Los Angeles, before joining Hunan University in 2018. His current research interests focus on the controllable synthesis and rational design of nanocarbon-supported single atom catalysts for energy and environmental applications.

石墨烯负载分子铁酞菁催化剂的形貌结构调控与氧还原催化应用

高曼[1†], 刘静静[1†], 叶龚兰[1*], 赵忠坤[2], 柳建斌[1], 何观朝[1], 龚智超[1], 黄康[1], 孙洪涛[2*], 费慧龙[1*]

摘要 分散在纳米碳基底上的分子催化剂由于具有明确的活性位点和结构可调的特点, 成为了一类独特的单原子催化剂, 有望代替贵金属催化剂用于电催化氧还原反应. 本文中, 我们开发了一种高活性氧还原催化剂, 该催化剂由均匀且密集分散在泡芙状石墨烯载体上的铁酞菁(FePc/PG)构成. 泡芙状石墨烯载体由于具有独特的皱褶和球状形貌, 具有较大的比表面积和多尺度的孔结构, 有利于FePc的高密度负载、活性位点的暴露和催化过程中传质效率的提高. 当用旋转圆盘电极评估性能时, FePc/PG表现出优异的半波电位, 达0.909 V (相对于可逆氢电极). 此外, 当用作气体扩散电极时, FePc/PG在高电流密度下表现出优异的高倍率和高功率性能. 这项工作为设计纳米碳材料的形貌以及高性能异相分子催化剂提供了有效的策略, 有望在多种能源转换和存储技术中得到应用.

